

# Probing the Local Structure and Mechanical Response of Nanostructures Using Force Modulation and Nanofabrication

W. J. Price,<sup>†</sup> P. K. Kuo,<sup>‡</sup> T. R. Lee,<sup>§</sup> R. Colorado, Jr.,<sup>§</sup> Z. C. Ying,<sup>||</sup> and G. Y. Liu\*<sup>†</sup>

Department of Chemistry, University of California, Davis, California 95616,  
Department of Physics, Wayne State University, Detroit, Michigan 48202,  
Department of Chemistry, University of Houston, Houston, Texas 77204-5003, and  
National Institute of Standards and Technology, Gaithersburg, Maryland 20899-8520

Received October 7, 2004. In Final Form: June 23, 2005

Nanostructures of self-assembled monolayers (SAMs) are designed and produced using coadsorption and nanografting techniques. Because the structures of these artificially engineered domains are predesigned and well-characterized, a systematic investigation is possible to study the mechanical responses to force modulation under atomic force microscope tips. Force modulation imaging reveals characteristic contrast sensitivity to changes in molecular-level packing, molecule chain lengths, domain boundaries, and surface chemical functionalities in SAMs. By means of actively tuning the driving frequency, the resonances at the tip–surface contact are selectively activated. Therefore, specific surface features, such as the edges of the domains and nanostructures or desired chemical functionalities, can be selectively enhanced in the amplitude images. These observations provide a new and active approach in materials characterization and the study of nanotribology using atomic force microscopy.

## I. Introduction

Atomic force microscopy (AFM) has been widely used in the fields of materials science and nanotribology because of its high spatial resolution, high force measurement sensitivity, simplicity of operation, and ability to image a wide range of materials under a variety of conditions.<sup>1–4</sup> Monitoring the vertical and lateral motions of the cantilever in either deflection- or interferometry-type AFM, topographic and frictional force images can be acquired simultaneously.<sup>3–9</sup> Additional modifications to this technique allow for the mapping of local polarization<sup>10</sup> and local magnetic anisotropies<sup>11</sup> in a surface. Mechanical properties such as elastic compliance and the viscoelastic behavior of thin films and surfaces have been probed at the nanometer scale, using force-modulation techniques.<sup>12–18</sup>

In the force-modulation mode, a sinusoidal voltage with controlled frequency and amplitude is applied to the piezoelectric tube that controls the sample position. The

cantilever response, manifested into an amplitude and a phase signal of the cantilever modulation, is recorded as a function of the driving signal (e.g., amplitude and frequency) and the locations of the tip on the surface.<sup>14–17</sup> Following the example of Overney et al., the local domains in phase-separated Langmuir–Blodgett films are clearly visualized from both the friction and elastic compliance images using the force-modulation technique.<sup>14</sup> Assuming that the tip–surface contact is Hertzian, local elasticity may be estimated from amplitude images.<sup>14</sup> This technique is particularly useful in characterization of hard–soft composite materials such as carbon fiber–epoxy composites,<sup>19,20</sup> calcium spots in cells,<sup>21</sup> inorganic thin films,<sup>22</sup> and block copolymers.<sup>23,24</sup>

Further studies using force-modulation AFM indicate that the amplitude and phase contrast depend on the driving frequency and amplitude, imaging medium, and nature of the surfaces under contact.<sup>25–27</sup> The tip–surface

<sup>†</sup> University of California.

<sup>‡</sup> Wayne State University.

<sup>§</sup> University of Houston.

<sup>||</sup> National Institute of Standards and Technology.

(1) Sarid, D. *Scanning Force Microscopy, with Applications to Electric, Magnetic and Atomic Forces*; Oxford University Press: New York, 1991.

(2) Binnig, G.; Quate, C. F.; Gerber, C. *Phys. Rev. Lett.* **1986**, *56*, 930–933.

(3) Frommer, J. *Angew. Chem., Int. Ed. Engl.* **1992**, *31*, 1298–1328.

(4) Quate, C. F. *Surf. Sci.* **1994**, *300*, 980–995.

(5) Carpick, R. W.; Salmeron, M. *Chem. Rev.* **1997**, *97*, 1163–1194.

(6) Ruan, J. A.; Bhushan, B. *J. Tribol.* **1994**, *116*, 378–388.

(7) Meyer, G.; Amer, N. M. *Appl. Phys. Lett.* **1988**, *53*, 1045–1047.

(8) Bhushan, B.; Israelachvili, J. N.; Landman, U. *Nature* **1995**, *374*, 607–616.

(9) Bhushan, B., Ed. *Handbook of Micro/Nanotribology*; CRC Press: Boca Raton, FL, 1995.

(10) Hu, J.; Xiao, X. D.; Salmeron, M. *Appl. Phys. Lett.* **1995**, *67*, 476–478.

(11) Florin, E. L.; Radmacher, M.; Fleck, B.; Gaub, H. E. *Rev. Sci. Instrum.* **1994**, *65*, 639–643.

(12) Carpick, R. W.; Ogletree, D. F.; Salmeron, M. *Appl. Phys. Lett.* **1997**, *70*, 1548–1550.

(13) Bar, G.; Rubin, S.; Parikh, A. N.; Swanson, B. I.; Zawodzinski, T. A.; Whangbo, M. H. *Langmuir* **1997**, *13*, 373–377.

(14) Overney, R. M.; Meyer, E.; Frommer, J.; Guntherodt, H. J.; Fujihira, M.; Takano, H.; Gotoh, Y. *Langmuir* **1994**, *10*, 1281–1286.

(15) Gould, S. A. C.; Drake, B.; Prater, C. B.; Weisenhorn, A. L.; Manne, S.; Kelderman, G. L.; Butt, H. J.; Hansma, H.; Hansma, P. K.; Magonov, S.; Cantow, H. J. *Ultramicroscopy* **1990**, *33*, 93–98.

(16) DeVecchio, D.; Bhushan, B. *Rev. Sci. Instrum.* **1997**, *68*, 4498–4505.

(17) Radmacher, M.; Tillmann, R. W.; Fritz, M.; Gaub, H. E. *Science* **1992**, *257*, 1900–1905.

(18) Radmacher, M.; Tillmann, R. W.; Gaub, H. E. *Biophys. J.* **1993**, *64*, 735–742.

(19) Dinelli, F.; Assender, H. E.; Takeda, N.; Briggs, G. A. D.; Kolosov, O. V. *Surf. Interface Anal.* **1999**, *27*, 562–567.

(20) Munz, M.; Sturm, H.; Schulz, E.; Hinrichsen, G. *Composites, Part A* **1998**, *29*, 1251–1259.

(21) Shiga, H.; Yamane, Y.; Ito, E.; Abe, K.; Kawabata, K.; Haga, H. *Jpn. J. Appl. Phys., Part 1* **2000**, *39*, 3711–3716.

(22) Resch, R.; Friedbacher, G.; Grasserbauer, M.; Kannianen, T.; Lindroos, S.; Leskela, M.; Niinisto, L. *Appl. Surf. Sci.* **1997**, *120*, 51–57.

(23) Pfau, A.; Janke, A.; Heckmann, W. *Surf. Interface Anal.* **1999**, *27*, 410–417.

(24) Matsui, H.; Kataoka, Y.; Shiraiishi, N. *Mokuzai Gakkaishi* **2000**, *46*, 475–482.

(25) Kiridena, W.; Jain, V.; Kuo, P. K.; Liu, G. Y. *Surf. Interface Anal.* **1997**, *25*, 383–389.

(26) Jourdan, J. S.; Cruchon-Dupeyrat, S. J.; Huan, Y.; Kuo, P. K.; Liu, G. Y. *Langmuir* **1999**, *15*, 6495–6504.

contact seems to exhibit resonance behavior with an external driving signal.<sup>26,28,29</sup> Under ambient conditions, the cantilever response is largely influenced by the capillary interaction at contact.<sup>8,30–33</sup> In a liquid medium where the capillary force is removed, the amplitude and phase images result from the viscoelastic behavior at the contact as well as mechanical resonances of the scanner assembly.<sup>26,34,35</sup>

Previously, our group has used nanoshaving to remove a selected area of octadecyltriethoxysilane (OTE) self-assembled monolayers (SAMs) on mica, which creates coexisting hard and soft areas.<sup>25</sup> Force-modulation AFM studies have revealed that the amplitude contrast flips at specific driving frequencies.<sup>26</sup> At 34 kHz the mica exhibits brighter contrast than the OTE, and the contrast is reversed at 43 kHz.<sup>26</sup> These observations suggest that (a) amplitude contrast depends on the driving frequency in addition to contact elasticity and (b) force-modulation imaging can be employed to probe local structures such as exposed mica areas within OTE SAMs.<sup>25</sup> Similar observations and conclusions have been reported for carbon fiber–epoxy composites<sup>19,20</sup> and Langmuir–Blodgett monolayers.<sup>11,22,36</sup> However, the prediction and quantification of the physical properties of these materials at the nanometer scale are still difficult and remain an active area of research.

A systematic investigation of the mechanical properties and responses of nanostructures of thin films is of fundamental importance in the development of microelectromechanical systems (MEMS) and nanoelectromechanical systems (NEMS). SAMs on gold/mica have been well characterized and well reported in the literature and thus provide a good model system for the coating of MEMS and NEMS. With the use of AFM-probe-based lithographic techniques, structures of controlled geometries can be precisely fabricated, therefore providing a good basis for systematic studies of the material properties of interest. These results provide a good hallmark for investigations of other thin films and real systems.

In this paper, we produce and characterize nanostructures of SAMs comprised of alkanethiols on Au(111) and study their mechanical responses to force-modulation AFM. 1-Alkanethiols form well-ordered structures on gold<sup>37–46</sup> that are well characterized.<sup>47</sup> The molecules adopt

a hexagonal and commensurate ( $\sqrt{3} \times \sqrt{3}$ )R30° structure on the Au(111) surface with a tilt angle of 30° from the surface normal.<sup>48</sup> Subtle structural heterogeneities of SAMs are engineered using coadsorption of mixed thiols<sup>49</sup> and nanografting.<sup>50</sup> Although the local domains within SAMs are similar, the force-modulation approach is sufficiently sensitive to the detailed structures within nanodomains, domain boundaries, and chemical functionality at the termini. More importantly, this study demonstrates that a selective probe of structural features at the nanometer scale can be achieved via force modulation at corresponding resonant frequencies.

## II. Experimental Section

**1. Sample Preparation.** Gold (Alfa Aesar, 99.999%) was deposited in a high-vacuum evaporator (Denton Vacuum Inc., model DV502-A) at a base pressure of  $2.6 \times 10^{-5}$  Pa onto freshly cleaved mica substrates (clear ruby muscovite, Mica New York Corp.). The mica was preheated to 325 °C before deposition by using two quartz lamps to enhance the mobility of gold during the formation of terraced Au(111) domains.<sup>51</sup> The typical evaporation rate was 0.3 nm/s, and the thickness of the gold films ranged from 150 to 200 nm. After removal from the vacuum evaporator the gold was immersed into freshly prepared thiol solutions.

The 1-alkanethiol adsorbates,  $\text{CH}_3(\text{CH}_2)_n\text{SH}$  (abbreviated as  $\text{C}_{n+1}\text{SH}$ ), and the hydroxy-terminated adsorbates 1-mercaptohexanol ( $\text{HOC}_6\text{SH}$ ) and 1-mercaptododecanol ( $\text{HOC}_{12}\text{SH}$ ) were purchased from Aldrich and used as received. The partially fluorinated adsorbate  $\text{CF}_3(\text{CF}_2)_9(\text{CH}_2)_2\text{SH}$ , was synthesized using previously reported procedures.<sup>52,53</sup>

Anhydrous ethanol and 2-butanol (99.6% purity) were purchased from Aldrich. Pure poly- $\alpha$ -olefin oil (PAO) was a gift from Ford Motor Co. Thiol solutions for SAM formation were prepared with concentrations ranging from 0.02 to 0.20 mM in solvents such as ethanol, 2-butanol, or PAO. Gold substrates were immersed into these solutions for a minimum of 48 h before imaging.

**2. AFM Imaging and Nanofabrication.** Our atomic force microscope utilizes a home-constructed deflection-type scanning head with a commercial electronic controller (RHK Technology, Inc., Troy, MI).<sup>54,55</sup> Sharpened  $\text{Si}_3\text{N}_4$  microcantilevers (MSCT) with a force constant of 0.1 N/m and a resonance frequency of 38 kHz (Veeco, Santa Barbara, CA) were used for this study. A laser beam is focused onto the back of the cantilever and deflected to a four-segment photosensitive detector which can monitor the vertical deflection and lateral twisting of the cantilever as the tip scans across the surface.

(27) Asif, S. A. S.; Wahl, K. J.; Colton, R. J.; Warren, O. L. *J. Appl. Phys.* **2001**, *90*, 1192–1200.

(28) Attard, P.; Schulz, J. C.; Rutland, M. W. *Rev. Sci. Instrum.* **1998**, *69*, 3852–3866.

(29) Ancyzkowski, B.; Kruger, D.; Babcock, K. L.; Fuchs, H. *Ultra-microscopy* **1996**, *66*, 251–259.

(30) Binggeli, M.; Mate, C. M. *J. Vac. Sci. Technol., B* **1995**, *13*, 1312–1315.

(31) Luna, M.; Colchero, J.; Baro, A. M. *Appl. Phys. Lett.* **1998**, *72*, 3461–3463.

(32) Colchero, J.; Storch, A.; Luna, M.; Herrero, J. G.; Baro, A. M. *Langmuir* **1998**, *14*, 2230–2234.

(33) Thundat, T.; Zheng, X. Y.; Chen, G. Y.; Warmack, R. J. *Surf. Sci.* **1993**, *294*, L939–L943.

(34) Nagayama, M.; Haga, H.; Tanaka, Y.; Hirai, Y.; Kabuto, M.; Kawabata, K. *Jpn. J. Appl. Phys., Part 1* **2002**, *41*, 4952–4955.

(35) Oshea, S. J.; Welland, M. E.; Pethica, J. B. *Chem. Phys. Lett.* **1994**, *223*, 336–340.

(36) Parrat, D.; Sommer, F.; Solleti, J. M.; Due, T. M. *J. Trace Microprobe Tech.* **1995**, *13*, 343–352.

(37) Mrksich, M.; Dike, L. E.; Tien, J.; Ingber, D. E.; Whitesides, G. M. *Exp. Cell Res.* **1997**, *235*, 305–313.

(38) Weisbecker, C. S.; Merritt, M. V.; Whitesides, G. M. *Langmuir* **1996**, *12*, 3763–3772.

(39) Tamchang, S. W.; Biebuyck, H. A.; Whitesides, G. M.; Jeon, N.; Nuzzo, R. G. *Langmuir* **1995**, *11*, 4371–4382.

(40) Liu, G. Y.; Fenter, P.; Chidsey, C. E. D.; Ogletree, D. F.; Eisenberger, P.; Salmeron, M. *J. Chem. Phys.* **1994**, *101*, 4301–4306.

(41) Biebuyck, H. A.; Bian, C. D.; Whitesides, G. M. *Langmuir* **1994**, *10*, 1825–1831.

(42) Kumar, A.; Biebuyck, H. A.; Whitesides, G. M. *Langmuir* **1994**, *10*, 1498–1511.

(43) Camillone, N.; Chidsey, C. E. D.; Liu, G. Y.; Scoles, G. *J. Chem. Phys.* **1993**, *98*, 3503–3511.

(44) Dubois, L. H.; Zegarski, B. R.; Nuzzo, R. G. *J. Chem. Phys.* **1993**, *98*, 678–688.

(45) Dubois, L. H.; Nuzzo, R. G. *Annu. Rev. Phys. Chem.* **1992**, *43*, 437–463.

(46) Sabatani, E.; Rubinstein, I.; Maoz, R.; Sagiv, J. *J. Electroanal. Chem.* **1987**, *219*, 365–371.

(47) Ulman, A. *An Introduction to Ultrathin Organic Films: From Langmuir-Blodgett to Self-Assembly*; Academic Press: Boston, 1991.

(48) Poirier, G. E.; Tarlov, M. *J. Langmuir* **1994**, *10*, 2853–2856.

(49) Delamarche, E.; Michel, B.; Gerber, C.; Anselmetti, D.; Guntherodt, H. J.; Wolf, H.; Ringsdorf, H. *Langmuir* **1994**, *10*, 2869–2871.

(50) Xu, S.; Miller, S.; Laibinis, P. E.; Liu, G. Y. *Langmuir* **1999**, *15*, 7244–7251.

(51) Xu, S.; Liu, G. Y. *Langmuir* **1997**, *13*, 127–129.

(52) Rondestvedt, C. S.; Thayer, G. L. *J. Org. Chem.* **1977**, *42*, 2680–2683.

(53) Graupe, M.; Koini, T.; Wang, V. Y.; Nassif, G. M.; Colorado, R.; Villazana, R. J.; Dong, H.; Miura, Y. F.; Shmakova, O. E.; Lee, T. R. *J. Fluorine Chem.* **1999**, *93*, 107–115.

(54) Salmeron, M.; Folch, A.; Neubauer, G.; Tomitori, M.; Ogletree, D. F.; Kolbe, W. *Langmuir* **1992**, *8*, 2832–2842.

(55) Xu, S.; Cruchon-Dupeyrat, S. J. N.; Garno, J. C.; Liu, G. Y.; Jennings, G. K.; Yong, T. H.; Laibinis, P. E. *J. Chem. Phys.* **1998**, *108*, 5002–5012.

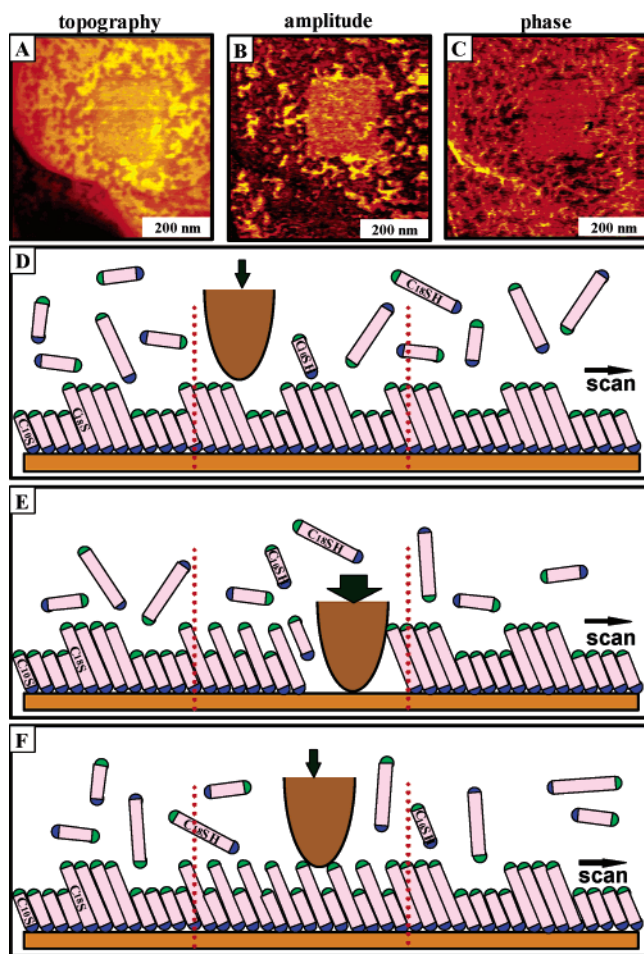


**Figure 1.** Preparation of various nanodomains within the same frame using coadsorption and nanofabrication techniques. The SAM matrix was prepared by immersing a gold substrate in a solution containing  $C_{10}SH:C_{18}SH = 10:1$ , total thiol concentration 0.02 mM. (A), (B), and (C) are the topography, amplitude, and phase images, respectively, simultaneously obtained from a  $600\text{ nm} \times 600\text{ nm}$  area. The force-modulation conditions were 32.50 kHz and 23 nm (peak to valley). The  $200\text{ nm} \times 200\text{ nm}$  square was grafted from the same solution. (D), (E), and (F) illustrate the three basic steps of nanografting. Nanografted regions are within the two dotted lines.

To investigate the sensitivity of force-modulation spectroscopy (FMS) and imaging (FMI) to changes in the molecular-level packing of organic thin films, nanodomains were prepared within SAMs. A SAM containing nanodomains with large and small segregations was produced using natural growth and nanografting processes, respectively. A specific example is shown in Figure 1A–C. The matrix SAM was prepared by immersing a gold substrate in a 0.02 mM solution of mixed thiols:  $C_{10}SH:C_{18}SH = 10:1$ . Immersing a gold substrate into a thiol solution containing a mixture of two different thiols often produces phase-separated nanodomains of various sizes within the SAM.<sup>56–58</sup> The size, geometry, and distribution of the nanodomains arise from the interplay of the self-assembly kinetics and thermodynamics. One can gain a certain degree of control by adjusting the total solution concentration, ratio of the two components, immersion time, solvent, and temperature. Under the preparation conditions specified in Figure 1,  $C_{10}SH$  and  $C_{18}SH$  molecules form domains with various shapes and sizes at the nanometer scale, as shown in the topographic, amplitude, and phase images. The matrix

consists of  $C_{18}SH$  areas (bright contrast) decorated by domains of  $C_{10}SH$  (dark areas). These domains range from 7 to 60 nm in lateral dimensions. In the topographic image, Figure 1A,  $C_{18}SH$  domains are 0.8 nm taller than the  $C_{10}SH$  domains, which is consistent with the difference in chain length and the known 30° chain tilt of alkanethiolate SAMs on gold.

In the central area of Figure 1A, a  $200\text{ nm} \times 200\text{ nm}$  square is produced using a nanografting operation.<sup>50,51,59,60</sup> Figure 1D–F schematically illustrates the basic steps of nanografting. The surface is first characterized with the AFM cantilever at low force. Once an appropriate fabrication area is located, typically a single Au(111) terrace, the load is then increased. At or above the threshold force, the tip will displace the thiol molecules from the gold surface via shearing during the scan. The threshold was determined at each experiment by imaging a  $5.0\text{ nm} \times 5.0\text{ nm}$  area while systematically increasing the load.<sup>51</sup> For pure SAMs, the periodicity of the SAMs (0.50 nm) was routinely revealed at low load until the threshold, above which the Au(111) lattice (0.30 nm) appeared. When this displacement is performed in a solution containing thiol molecules, the molecules in solution will self-assemble onto the newly exposed gold areas, forming a nanostructure following the trajectory of the scan. The load is then decreased to allow characterization of the newly formed nanostructure. High-resolution images revealed that thiols in these nanostructures are also closely packed.<sup>50</sup>

For this investigation, the matrix consisted of a two-component mixed SAM. Nanografting was performed within the SAM using a solution containing the aforementioned thiol mixture. Our research group has demonstrated that the domain structure in the nanografted areas is different from that in the matrix.<sup>61</sup> Specifically, the  $C_{10}SH$  and  $C_{18}SH$  molecules appear less segregated at the molecular level than those in the matrix. The detailed investigation of the mechanism and structure of naturally grown versus nanografted mixed SAMs is beyond the focus of this paper and will be discussed elsewhere.<sup>61</sup> The important outcome is that we have produced nanodomains that are relatively segregated in the matrix SAM and mixed at the molecular level in the nanografted areas for force-modulation studies. This observation is reproduced for mixed SAMs over a wide range of concentration and molar ratio.<sup>61</sup> The SAMs and nanostructures are sufficiently stable in the duration of the force-modulation experiments, typically 10 h.

**3. Force-Modulation Spectroscopy.** FMS can be acquired with the setup in Figure 2. Once the AFM tip is positioned on top of the structure of interest, the computer-controlled function generator initiates a frequency sweep. The function generator output is provided as a reference input to the lock-in amplifier, driving the piezo tube along the surface-normal direction. The tip responses at the tip–surface contact are detected by the photodiode and amplified by the lock-in amplifier. The amplitude and phase signals from the amplifier are then processed by a DAC board (National Instruments PCI-6024E multiple I/O and DAQ interfaced with a CB-68LP I/O connector block) and plotted as a function of the sweeping frequency.

**4. Force-Modulation Imaging.** In addition to conventional AFM imaging and force-modulation spectroscopy, our setup shown in Figure 2 is able to conduct FMI. For FMI, the sample is modulated with a sinusoidal signal of a fixed frequency in the  $z$  direction. The frequency  $f$  and amplitude  $\Delta z$  are controlled by the lock-in amplifier. The modulation signal is normally set at frequencies above the response of the feedback circuit (several kilohertz) to minimize the coupling with the feedback circuit. The cantilever follows the sinusoidal motion when the tip is in contact with the surface. During imaging, the amplitude and phase response of the cantilever are detected by the lock-in amplifier and then recorded as a function of the tip position. The response of the cantilever is sensitive to the local tip–surface contact. Three channels of data are acquired simultaneously, which produce a topographic image and its corresponding amplitude and phase images for the forward and reverse scanning directions (six pages total). There is a slight time lag between

(56) Hayes, W. A.; Kim, H.; Yue, X. H.; Perry, S. S.; Shannon, C. *Langmuir* **1997**, *13*, 2511–2518.

(57) Folkers, J. P.; Laibinis, P. E.; Whitesides, G. M.; Deutch, J. J. *Phys. Chem.* **1994**, *98*, 563–571.

(58) Folkers, J. P.; Laibinis, P. E.; Whitesides, G. M. *J. Adhes. Sci. Technol.* **1992**, *6*, 1397–1410.

(59) Liu, G. Y.; Xu, S.; Qian, Y. L. *Acc. Chem. Res.* **2000**, *33*, 457–466.

(60) Xu, S.; Laibinis, P. E.; Liu, G. Y. *J. Am. Chem. Soc.* **1998**, *120*, 9356–9361.

(61) Yu, J. J.; Kuo, P. K.; Schatz, G. C.; Ryu, S.; Yang, G.; Li, X.; Liu, G., manuscript in preparation.

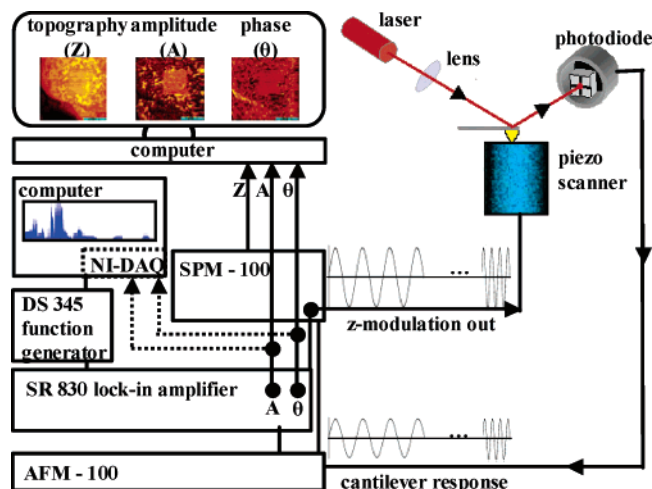


**Figure 2.** Schematic diagram of the AFM setup for FMI and FMS. The instrument used consists of a home-built deflection-type atomic force microscope controlled by commercial electronics and software (RHK Technology, Inc.). A lock-in amplifier (SRS SR830), a function generator (SRS DS345), and a National Instruments measurement studio with an NI-DAQ card were also utilized to provide the modulation signal and selective amplification and to collect and process the data.

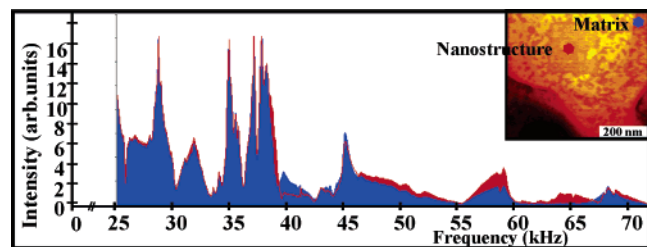


**Figure 3.** Force-modulation spectra of the system described in Figure 1 at tip– $C_{10}SH$  and tip–nanostructure contacts. The modulation amplitude for these spectra was 7.8 nm, and the frequency was swept from 25.00 to 72.00 kHz. The total scan area for the inset was 600 nm  $\times$  600 nm with a 200 nm  $\times$  200 nm nanostructure in the center.

the topographic and the amplitude and phase images, on the order of 3–4 ms, due to the conversion of the photodiode signals to amplitude and phase by the lock-in amplifier.

Most of our measurements were taken under low force; thus, there is little frictional component. For measurements taken at higher force, attempts were made to minimize the interaction of the normal and lateral signals. The control electronics employs a decoupling circuitry to compensate the coupling of normal and lateral signals from the cantilever. The cantilever deformation in the normal and lateral directions was recorded during approach and retreat of the AFM tip. We adjusted the lateral deformation electronically while acquiring the deformation signal until the lateral signal diminished. In our experiments all measurements were done in solution to minimize the tip–sample adhesion. Since relatively soft cantilevers were used, a decoupling function was employed. As a result the coupling between the normal and lateral photodiode signals is reduced by 95–99%.

### III. Results and Discussion

**1. Probing Lateral Heterogeneity Using FMS and FMI.** As reported previously, tip–surface contact exhibits resonances under force modulation.<sup>26</sup> Thus, force-modulation spectroscopy is acquired for each experiment to qualitatively survey the resonance behavior of the system under investigation. In the phase-separated mixed SAMs shown in Figure 1, modulation spectra were taken at two distinct contacts (see Figure 3): at the matrix above a  $C_{10}SH$  domain and at the nanostructure, where the  $C_{10}SH$  and  $C_{18}SH$  are more mixed on a molecular level.

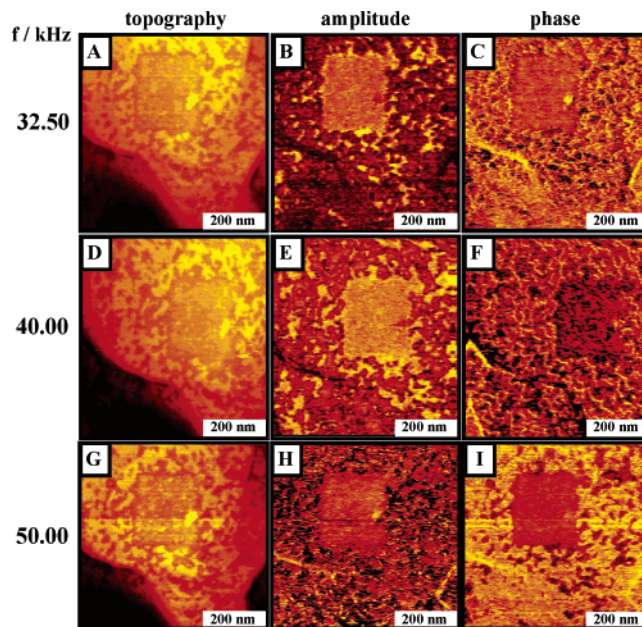


**Figure 4.** Force-modulation imaging of the system described in Figure 1 at frequencies of 32.50, 40.00, and 50.00 kHz. The modulation amplitude was 7.8 nm (maximum), and the total scan area was 600 nm  $\times$  600 nm with a 200 nm  $\times$  200 nm nanostructure in the center.

The peaks shown in Figure 3 arise from three sources: (a) intrinsic vibrations of the cantilever, (b) mechanical resonances of the sample and cantilever holder assemblies, and (c) resonances arising from the tip–surface contact. In air, most peaks diminish when the tip is retracted, with only cantilever resonance visible, i.e., 28.00 kHz in this measurement. In 2-butanol, most of the peaks still remained when the cantilever was completely retracted from the surface. The resonances in contact typically are stronger than those from the out of contact situation, hinting that the nature of these resonances arises from the inherent mechanical vibrations of the sample assembly. There are, however, peaks appearing only upon contact, 29.50, 44.30, and 64.20 kHz, which are attributed to resonances of the tip–surface contact.

Note that FMS varies with the lateral location, e.g., tip–matrix versus tip–nanostructure as shown in Figure 3. FMS is therefore sensitive to the lateral heterogeneity of the SAMs. Since the tip–SAM contact is viscoelastic in nature, the FM spectra also depend on the speed of the frequency sweeps. To obtain a consistent contact, slow imaging speeds were selected to probe differences in surface structure, i.e., using FMI to map out the surface at one given frequency. Individual images were acquired at frequencies ranging from 22.00 to 55.00 kHz. At 32.50 kHz, parts A–C of Figure 4 show phase-segregated nanodomains in the matrix area of  $C_{10}SH$  and  $C_{18}SH$  that are clearly distinguishable in the topography, amplitude, and phase images. In the topographic image, the tallest structural features, i.e., the  $C_{18}SH$  nanodomains in the matrix, display the brightest contrast. Amplitude image contrast (brightness) represents the response of the tip–surface contact to modulation. This is intrinsically different from the topographic image where the brightness corresponds to the sample height. The amplitude contrast changes in the presence of resonances. In the amplitude images, the  $C_{10}SH$  nanodomains in the matrix exhibit the brightest contrast. This amplitude response is 1.0 V higher than that of the central nanostructure where  $C_{10}SH$  and  $C_{18}SH$  are more uniformly mixed at the molecular level. The  $C_{10}SH$  domain is 2.0 V higher than the  $C_{18}SH$

nanodomains in the matrix. This quantitative difference demonstrates that force-modulation imaging is sufficiently sensitive to the molecular-level structural differences: pure C<sub>10</sub>SH and pure C<sub>18</sub>SH domains versus molecularly mixed areas.

At 40.00 kHz, shown in Figure 4D–F, nanodomains of C<sub>10</sub>SH and C<sub>18</sub>SH in the matrix region are again clearly distinguishable in the topography, amplitude, and phase images. The amplitude response for the tip–C<sub>10</sub>SH contact is 0.40 V higher than that of the nanostructure where molecular level mixing is approached and 0.80 V higher than that of the tip–C<sub>18</sub>SH contact. At both 32.50 and 40.00 kHz, C<sub>10</sub>SH nanodomains in the phase-segregated matrix area display enhanced contrast. At 50.00 kHz, shown in Figure 4G–I, C<sub>18</sub>SH nanodomains in the matrix are resonantly enhanced and exhibit an amplitude response that is 0.50 V higher than that of the nanostructure and 1.05 V higher than that of the C<sub>10</sub>SH matrix nanodomains.

The data shown in Figure 4 demonstrate that the force-modulation amplitude and phase images correspond well with molecular-level structures shown in the topography. In addition, the contrast in the amplitude and phase images is sharper and depends on the modulation frequency. The order of amplitude contrast from the highest to the lowest is C<sub>10</sub>SH domain > nanostructure with molecular mixing > C<sub>18</sub>SH domain at both 32.50 and 40.00 kHz. The order is reversed at 50.00 kHz. A careful examination of Figure 4 reveals that the domain boundaries are better identified in the amplitude images than in the topographic images. This observation may be rationalized by considering the imaging mechanisms. Topography reflects the height of the surface features as detected by an AFM tip and is thus more susceptible to tip-geometry convolution and feedback circuitry. The force modulation amplitude and phase, on the other hand, reflect contact dynamics or mechanical responses under modulation, whose signals do not go through the feedback electronics.

**2. Probing the Domain Boundaries Using Force-Modulation Imaging.** To test the sensitivity of force modulation to the boundaries of the nanostructures, we first prepared a series of C<sub>18</sub>SH nanostructures in various sizes and geometries within a C<sub>6</sub>SH matrix using nano-grafting. These nanostructures are shown in Figure 5. The geometry of these nanostructures varies with lines, squares, rectangles, and a polygon shaped like a “light-house”. The C<sub>18</sub>SH nanostructures can be identified in the topographic images because they measure taller than the C<sub>6</sub>SH matrix.

Figure 5 shows images of these engineered nanostructures acquired at 3.68 nm modulation amplitude and two characteristic frequencies, 19.00 kHz (top) and 21.00 kHz (bottom). The topographic images clearly show the location of the C<sub>18</sub>SH nanostructures, which are taller than the C<sub>6</sub>SH matrix. The theoretical height difference between C<sub>6</sub>SH regions and C<sub>18</sub>SH regions for close-packed and well-ordered SAMs is 1.5 nm,<sup>62</sup> which is in good agreement with the measured values indicated by the cursor plots (Figure 5a,d). At 19.00 kHz, the edges of the nanostructures exhibit brighter contrast in both the amplitude and phase images, due to a resonance at the tip–surface contact. Furthermore, the resonance frequency of the edges appears to be independent of the pattern size or geometry.

The full width at half-maximum (fwhm) of these edges in the amplitude images was measured to be 5.5 nm (see the cursor in Figure 5b). Using a nearest neighbor distance

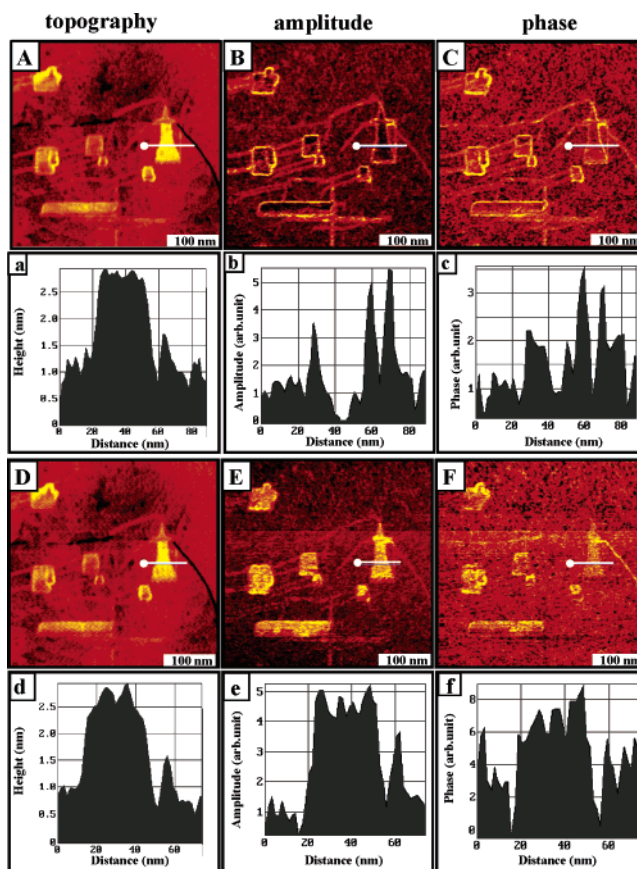


**Figure 5.** Force-modulation imaging of various C<sub>18</sub>SH nanostructures fabricated into a C<sub>6</sub>SH SAM matrix. Images were taken at 4.4 nN, with a scan area of 400 nm × 400 nm. Modulation conditions: 19.00 kHz and 3.68 nm (top) and 21.00 kHz and 3.68 nm (bottom). Corresponding cursor plots are displayed under each image.

of 0.5 nm for thiol SAMs,<sup>62</sup> we estimate that the edges or boundaries consist of 11 thiol molecules. The radius of the AFM tip used in this experiment was estimated to be 6.71 nm following the procedure described previously.<sup>63</sup> *This study demonstrates that FMI can be used to quantify the boundaries of the domains or edges of the structural features.*

At 21.00 kHz, the bulk of the nanostructures exhibits relatively strong resonances. Correspondingly, the edges and matrix fade in the background. The size of each nanostructure revealed in the amplitude and phase images reflects the dimensions of the 2D bulk of each pattern. Under this particular FMI condition, the nanostructures are selectively enhanced.

The data shown in Figure 5 serve as examples of a general trend that borders of the nanostructures are resonantly enhanced at lower frequencies than the bulk nanostructure. We have performed systematic studies of force modulation over a frequency range from 19.00 to 45.00 kHz, with modulation amplitudes varying from 0.92 to 9.2 nm. Two average forces were applied: 4.4 and 14.4 nN. At 0.92 nm modulation amplitude and 4.4 nN imaging force, multiple resonance peaks for the nanostructure borders are observed at frequencies in a range from 19.00 to 23.00 kHz, and resonance responses for the bulk occur from 25.00 to 45.00 kHz. Increasing the modulation amplitude to 3.68 nm while keeping the imaging force at 4.4 nN, the resonance for the borders is observed only at

(62) Ulman, A. *An Introduction to Ultrathin Organic Films: From Langmuir-Blodgett to Self-Assembly*; Academic Press: San Diego, 1991.

(63) Xu, S.; Amro, N. A.; Liu, G. Y. *Appl. Surf. Sci.* **2001**, *175*, 649–655.

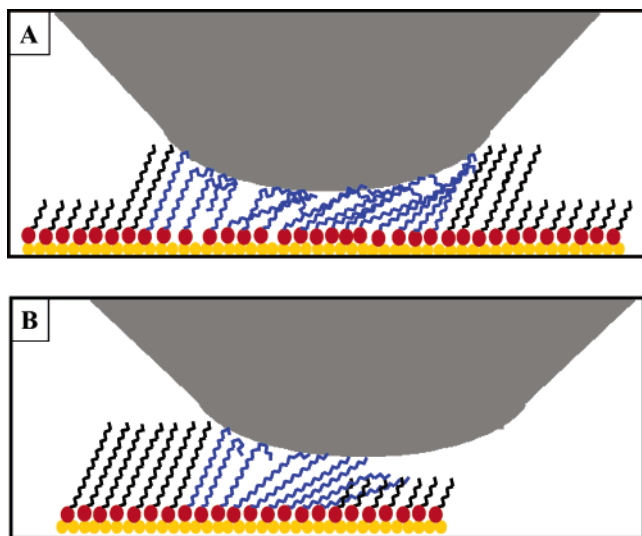


**Figure 6.** Scheme illustrating the behavior of SAM nanostructures under force modulation. Molecules deformed at contact during FM are highlighted in blue. (A) Bulk nanostructures are shown under a compression cycle, where molecules may exhibit higher than 30° tilt angles and/or a terminal gauche conformation. The initial closely packed structures are reestablished during the release cycle. (B) Molecules on the edges of the nanostructures under a compression cycle may tilt more or exhibit a gauche conformation. The deformation is greater than that of the bulk due to more free volume at the boundary.

19.00 kHz, the lowest frequency used in this study. The bulk nanostructure exhibits multiple resonances at frequencies of 20.00 kHz and higher. A further increase of the modulation amplitude leads to the observation of resonance responses only from the bulk nanostructure.

The observed difference between the bulk nanostructures and boundaries may be rationalized qualitatively using the scheme presented in part A and B, respectively, of Figure 6. Since resonances are observed in the frequency range of tens of kilohertz, the motions/modes involved are relatively soft in comparison to the normal modes of molecules such as C–H stretching or C–C stretching. The normal modes of the vibrational and rotational motions of individual molecules can therefore be ruled out. Possible candidates must be mechanical in nature and could include motions involving groups of molecules such as deformation–relaxation, phonon motion, and hydrodynamic forces in a liquid environment.<sup>18,26,64</sup> The bulk areas of the SAM and of the nanostructure consist of thiols in a closely packed structure. Below the fabrication threshold and under force modulation, molecules under the tip may tilt more, interdigitate with the surrounding SAM, or form terminal gauche conformations. Since topographic images exhibit the predicted height, the molecules presumably recover to their initial positions upon releasing or reducing the local pressure. The time difference between deformation and recovery reflects the viscoelastic behavior of the contact.<sup>14,18,65,66</sup> The edges of the C<sub>18</sub>SH patterns likely possess a greater degree of conformational flexibility and space for deformation. Similar edge effects have been observed for isolated C<sub>16</sub>SH domains on gold.<sup>67</sup> At the edges of the nanostructures, the molecules have more space to

(64) Rabe, U.; Kopycinska, M.; Hirsekorn, S.; Arnold, W. *Ultrasonics* **2002**, *40*, 49–54.

(65) Jayalakshmi, Y.; Ozanne, L.; Langevin, D. *J. Colloid Interface Sci.* **1995**, *170*, 358–366.

(66) Overney, R. M.; Bonner, T.; Meyer, E.; Reutschi, M.; Luthi, R.; Howald, L.; Frommer, J.; Guntherodt, H. J.; Fujihara, M.; Takano, H. *J. Vac. Sci. Technol., B* **1994**, *12*, 1973–1976.

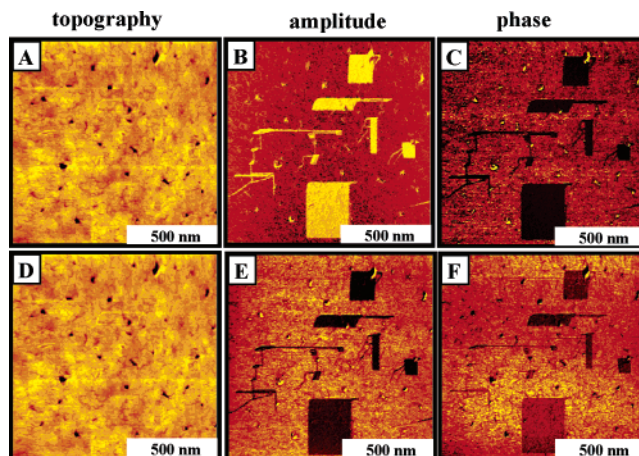


**Figure 7.** Force-modulation imaging of a 1500 nm × 1500 nm area of C<sub>12</sub>SH nanostructures fabricated into a HOC<sub>12</sub>SH matrix. (A), (B), and (C) are topography, amplitude, and phase images, respectively, acquired at a modulation frequency of 37.00 kHz and an amplitude of 3.25 nm. (D), (E), and (F) are topography, amplitude, and phase images, respectively, for the same area taken at a frequency of 34.00 kHz and an amplitude of 3.25 nm.

tilt and form gauche conformations in comparison to the densely packed regions. Therefore, the edges exhibit softer and more viscoelastic behavior than the bulk areas. We believe additional studies, such as molecular dynamics and finite element analysis simulations, are necessary to fully understand the contrast mechanism(s) in FMI.

**3. Sensitivity of FMI to Local Chemical Functionalities.** The sensitivity of FMI to changes in the local surface functionality has also been studied. For this purpose, a series of nanostructures of C<sub>12</sub>SH ranging in size from 15 nm × 15 nm to 300 nm × 300 nm were fabricated into a matrix SAM of HOC<sub>12</sub>SH. These two molecules were chosen because they have the same chain length, but different terminal groups. While displaying the same height in the topographic image (Figure 7A,D), the difference in termini is clearly visible in the amplitude and phase images.

The amplitude and phase images clearly show the locations of the nanostructures fabricated into the matrix. At 37.00 kHz, the nanostructures display a higher contrast than the matrix in the amplitude image as shown in Figure 7B. At this frequency, the amplitude response of the nanostructures is 0.30 V higher than that of the surrounding matrix SAM. At 34.00 kHz, shown in Figure 7E, the matrix has a 0.35 V higher amplitude response than the nanostructures engineered into this matrix. These observations demonstrate that one can use the driving frequency in FMI to selectively enhance a designated chemical functionality.

It has been reported that frictional force exhibits varying contrast depending upon the chemical functionality.<sup>5,14,68–73</sup> Most of our experiments use SAMs immersed in liquids and under low imaging forces, in contrast to the relatively high loading forces in most of the frictional measure-

(67) Barrena, E.; Ocal, C.; Salmeron, M. *J. Chem. Phys.* **2000**, *113*, 2413–2418.

(68) Dedkov, G. V. *Phys. Status Solidi A* **2000**, *179*, 3–75.

(69) Landman, U.; Luedtke, W. D.; Ouyang, J.; Xia, T. K. *Jpn. J. Appl. Phys., Part 1* **1993**, *32*, 1444–1462.

(70) Wang, J. F.; Rose, K. C.; Lieber, C. M. *J. Phys. Chem. B* **1999**, *103*, 8405–8409.

(71) Drummond, C.; Israelachvili, J. *Macromolecules* **2000**, *33*, 4910–4920.

(72) Yamada, S.; Israelachvili, J. *J. Phys. Chem. B* **1998**, *102*, 234–244.

(73) Noy, A.; Frisbie, C. D.; Rozsnyai, L. F.; Wrighton, M. S.; Lieber, C. M. *J. Am. Chem. Soc.* **1995**, *117*, 7943–7951.

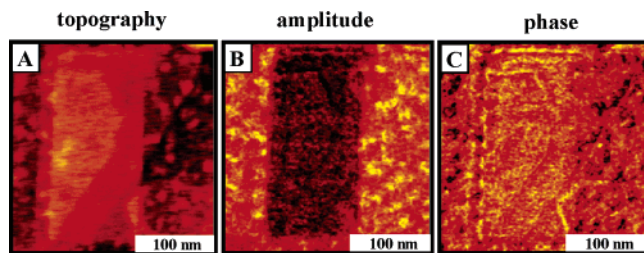


**Figure 8.** Force-modulation imaging of SAMs with multiple surface functionalities. (A), (B), and (C) are topography, amplitude, and phase images, respectively, for a two-component SAM formed from the coadsorption of HOC<sub>6</sub>SH and C<sub>10</sub>SH, freshly prepared from a mixed thiol solution of HOC<sub>6</sub>SH:C<sub>10</sub>SH = 2:1. The total concentration was 0.02 mM. Within this matrix a 120 nm × 225 nm nanostructure of CF<sub>3</sub>(CF<sub>2</sub>)<sub>9</sub>(CH<sub>2</sub>)<sub>2</sub>SH was nano-grafted at the central region. The total image area is 260 nm × 260 nm, acquired at a frequency of 36.80 kHz and an amplitude of 6.0 nm.

ments.<sup>74</sup> Under such low loads there is very little lateral force signal detectable. Thus, the contact differences found are mostly due to the FM resonances in the normal direction. In contrast to lateral force imaging, FMI can selectively enhance one surface functionality over another, due to the differences in the viscoelastic contributions of the tip–surface contact. *This makes FMI a more active probe in differentiating surface features since, by using different driving frequencies, one can enhance the resonances of the desired surface features.*

As a further demonstration of this sensitivity to local chemical functionality a SAM with three different surface chemical functionalities was engineered. First a mixed SAM was formed by the coadsorption of HOC<sub>6</sub>SH and C<sub>10</sub>SH, resulting in a phase-segregated structure. This sample was prepared by the immersion of a gold substrate into a 0.02 mM 2-butanol solution of these two components with a 2:1 ratio of HOC<sub>6</sub>SH to C<sub>10</sub>SH. A nanostructure containing a third chemical functionality, CF<sub>3</sub>(CF<sub>2</sub>)<sub>9</sub>(CH<sub>2</sub>)<sub>2</sub>SH, was fabricated into this phase-segregated matrix. The phase-segregated nanodomains surrounding the central nanostructure are evident in Figure 8A. The surface topography is one in which C<sub>10</sub>SH nanodomains and the CF<sub>3</sub>(CF<sub>2</sub>)<sub>9</sub>(CH<sub>2</sub>)<sub>2</sub>SH nanostructure appear brighter (taller) than the HOC<sub>6</sub>SH nanodomains. The location of these domains can also be readily identified in the corresponding amplitude and phase images in parts B and C, respectively, of Figure 8. Each of the three terminal chemical functionalities CH<sub>3</sub>–, HO–, and CF<sub>3</sub>– exhibit distinct and characteristic responses in the amplitude and phase images. At frequencies below 25.00 kHz, the HOC<sub>6</sub>SH nanodomains in the matrix SAM display multiple resonances and exhibit a higher amplitude response than the C<sub>10</sub>SH nanodomains. Above 25.00 kHz, however, the C<sub>10</sub>SH nanodomains exhibit a higher amplitude response than the HOC<sub>6</sub>SH nanodomains. Across the range of frequencies probed the CF<sub>3</sub>(CF<sub>2</sub>)<sub>9</sub>(CH<sub>2</sub>)<sub>2</sub>SH nanostructure had a lower amplitude response than the surrounding matrix nanostructures. The images shown in Figure 8 were obtained at 36.80 kHz. At this frequency,

the C<sub>10</sub>SH nanodomains have an amplitude response 0.015 V higher than that of the HOC<sub>6</sub>SH nanodomains and 0.030 V higher than that of the CF<sub>3</sub>-terminated nanostructure. FMI images clearly can distinguish multiple chemical functionalities. The difference in the contrast of the amplitude and phase images may be altered using a variation in the driving frequency.

#### IV. Conclusions

Using coadsorption and nanografting techniques, nano domains of mixed SAMs are formed and engineered, respectively. These well-characterized nanostructures have been used to investigate local mechanical responses under force modulation. Subtle structural differences in SAM nanostructures, such as lateral heterogeneity, functionalities at the termini, and boundaries and edges of the nanodomains, can be clearly resolved in force-modulation imaging.

Force-modulation imaging can be used to better quantify the degree of phase segregation than topographic images, because the amplitude and phase images are less sensitive to tip convolution effects. By tuning the driving frequencies to a local tip–surface resonance frequency, specific surface features, including the boundaries of the domains, edges of the nanostructures, and chemical functionalities, can be selectively enhanced in amplitude and phase images. This approach provides an active tool to materials characterization at the nanometer scale and in the study of nanotribology by AFM. Hopefully, this initial study using well-characterized nanostructures can attract more theoretical and simulation work to explore further the origins of the observed resonances and to take advantage of the selective enhancement.

**Acknowledgment.** We greatly appreciate the technical assistance of and stimulating discussions with Jingjiang Yu, Xue Li, and Amanda Price at the University of California, Davis. We also thank Dr. Stephen Hsu at the National Institute of Standards and Technology (NIST) for many helpful discussions and Dr. R. Carter at Ford Motor Co. for the PAO solvent. This work was supported by the University of California, Davis, NSF (through a CPIMA seed fund by Stanford University), and the Nanotechnology Initiative of the National Institute of Standards and Technology, Materials Science and Engineering Laboratory, in conjunction with the NIST nanotribology research program. Additional support for T.R.L. was provided by the Robert A. Welch Foundation (Grant E-1320) and the Texas Advance Research Program (Grant 003652-0307-2001). W.J.P. acknowledges support from the Tyco Electronics Graduate Fellowship in Functional Materials. (The following is a statement per the request of the NIST grant: Certain commercial equipment, instruments, or materials are identified in this paper to specify the experimental procedure adequately. Such identification is not intended to imply recommendation or endorsement by the National Institute of Standards and Technology, nor is it intended to imply that the materials or equipment identified are necessarily the best available for the purpose.)

(74) Wilbur, J. L.; Biebuyck, H. A.; Macdonald, J. C.; Whitesides, G. M. *Langmuir* **1995**, *11*, 825–831.